

# Decoupling the electrical resistivity contribution of grain boundaries in dilute Fe-alloyed Cu thin films

Hanna Bishara<sup>a,b,\*</sup>, Lena Langenohl<sup>a</sup>, Xuyang Zhou<sup>a</sup>, Baptiste Gault<sup>a,c</sup>, James P. Best<sup>a</sup>, Gerhard Dehm<sup>a,\*</sup>

<sup>a</sup> Max-Planck-Institut für Eisenforschung GmbH, Max-Planck-Straße 1, 40237 Düsseldorf, Germany

<sup>b</sup> Department of Material Science and Engineering, Tel Aviv University, Ramat Aviv 6997801, Tel Aviv, Israel

<sup>c</sup> Department of Materials, Royal School of Mines, Imperial College, Prince Consort Road, London SW7 2BP, UK

## ARTICLE INFO

### Keywords:

Electrical resistivity  
Grain boundary  
Sputtering  
Grain growth  
Thin films

## ABSTRACT

To study the role of chemical composition on the resistivities of grains and grain boundaries (GB) for dilute Fe-alloyed Cu thin films, Cu films with grain sizes varying over three orders of magnitude and compositions of 0.025 and 0.25 at.% Fe were prepared by magnetron co-sputtering. Character, morphology and compositions of bulk and GBs were studied using electron backscatter diffraction, transmission electron microscopy and atom probe tomography, respectively. The specific resistivities of both individual GBs and within grains were obtained through local electrical measurements assisted by micromanipulation *in situ* within a scanning electron microscope. In addition, global resistivity characterisation of the thin films allowed for calculation of the GB reflection coefficient. A decoupling of GB and grain interior resistivities is found with alloying, where the GB resistivity increases by an order of magnitude while the grain interior is affected only to a minor extent in comparison.

Alloying of pure elemental metals is required to enhance the mechanical performance of conductive materials employed in applications like overhead power lines, automobile industry, and high-speed railway conductors [1–4]. However, alloying is accompanied with an increase of electron scattering centres within the material, which suppresses its electrical properties and leads to high energy dissipation and Joule heating during electricity transmission. Grain boundaries (GBs) are among the dominant defects that increase the resistivity of alloys [5,6]. While GB resistivity has been studied in pure metals [7–11], it has not received a sufficient attention in alloys - likely due to the chemical complexity, where segregation and precipitation effects are involved. Density functional theory (DFT) calculations show that the GB resistivity of a Cu alloy might increase by three-fold, depending on the alloying element and GB type [12]. Experimental studies usually consider the GB resistivity as an accumulated property of entire boundaries within the material [13,14]. However, quantification of the resistivity increase for an individual GB due to alloying and correlating it to the GB character is still missing. Therefore, separating the resistivities of GBs from the grain interior by direct measurements will improve the understanding for electrical properties of alloys.

The contribution of GB to the resistivity of a material may be

quantified by two values [15]: the GB resistivity  $\gamma_{GB}$  representing the resistivity which originates from a GB per unit area [16], and the GB reflection coefficient  $R$  indicating the probability of an electron to be scattered by a GB [17]. Recently, local electrical measurements were introduced to directly measure  $\gamma_{GB}$  in thin films [18]. This technique requires columnar grains of a few micrometres diameter in the film, which are often obtained by abnormal grain growth. Such a requirement is typically fulfillable in pure metallic films [19,20], but is challenging in alloys due to GB pinning caused by solutes and other effects [21,22]. Nevertheless, abnormal grain growth has been observed for several multi-component material thin films [23–26].

Dilute Fe-Cu alloys exhibit relatively high thermal and electrical conductivities, dominated by the Cu matrix, combined with high strength provided by the Fe solute [27], and provide a model system for bcc alloying elements in the fcc Cu. Since Fe is insoluble in Cu and intermetallic phases are not formed, it tends to precipitate even for dilute compositions. Coherent fcc precipitates are initially nucleated and grow either with plate-like [28] or spherical morphologies [29–31]; the bcc Fe phase appears after aging or mechanical deformation. The resistivities of Fe-alloyed Cu thin films were reported to correlate with grain size more than with composition [32]. However, the resistivity

\* Corresponding author.

E-mail addresses: [hbishara@tauex.tau.ac.il](mailto:hbishara@tauex.tau.ac.il) (H. Bishara), [g.dehm@mpie.de](mailto:g.dehm@mpie.de) (G. Dehm).

**Table 1**

List of FeCu films grown on (0001) Sapphire with the corresponding deposition parameters. All samples were annealed at 350°C for 3 hr after deposition. OR-I and OR-II are the orientation relationship between film and substrate (see text for details).

#	Co-sputtering	Deposition temperature (°C)	Fe composition	Average grain size	Orientation relationship
1	Continuous	25	0.25 at%	190 nm	OR-I
2	Continuous	350	0.25 at%	690 nm	OR-I + OR-II
3	Discontinuous	350	0.025 at%	> 20 $\mu\text{m}$	OR-II

was globally assessed while the individual contributions of both GBs and solid solutions were not considered.

Fe-Cu dilute solution thin films were prepared by co-sputtering a pure Cu target (99.999%) using a RF cathode at 250 W, and 5 at.% Fe-alloyed Cu target (Mateck) sputtered with a DC cathode at 15 W. Depositions were performed on (0001) planes of Sapphire substrates (Mateck) at  $1 \cdot 10^{-8}$  mbar base pressure, deposition pressure  $5 \cdot 10^{-3}$  mbar, and Ar flow of 20 sccm for 40 mins resulting in nominal 500 nm thick films. A co-sputtering process in the stated conditions yielded Cu thin films with a calculated nominal composition of  $\sim 0.2$  at.% Fe. An estimation of the composition is given in the Supplementary Materials. Table 1 presents the three deposition protocols considered in this work: continuous co-sputtering at room temperature (film #1), continuous co-sputtering at 350°C (film #2), and discontinuous co-sputtering at 350°C (film #3). All samples were post-annealed immediately after the deposition in the same vacuum chamber at 350°C for 3 hr. The first two protocols concern operation of both sputtering cathodes during the whole deposition. However, in the third protocol, only the pure-Cu cathode was operated during the whole process while Fe

alloyed-Cu sputtering was active only partially as illustrated in Fig. 1, creating a layered-like film. The motivation behind this deposition approach is to create an interface between pure Cu and Sapphire, leading to grain growth via an epitaxial driving force [18,33]. Post-annealing of film #3 leads to Fe diffusion mainly along the GBs, while the Fe distribution in the annealed film is discussed below experimentally and by a diffusion calculation.

Microstructures of the films were initially assessed through electron backscatter diffraction (EBSD) in a scanning electron microscopy (SEM) (Auriga, Zeiss) using an EDAX detector and electron acceleration voltage of 15 kV. Data was analysed with OIM Analysis software. The diffraction patterns of  $\alpha\text{-Al}_2\text{O}_3$  were obtained from an exposed Sapphire surface on the wafers (area underneath the clamps during the deposition) and acquired in the same EBSD scan batch as the film.

The average grain sizes of the films presented in Table 1 are deduced from the EBSD-resolved inverse pole figure maps shown in Fig. 2, where the colours indicate the relative in-plane orientations. In films #1 and #2, a grain growth stagnation is achieved at a relatively small-grain size, likely due to a Zener drag effect from the clustering of Fe atoms – as seen in the atom probe tomography (APT) reconstructions for film #1 in Fig. S1. In contrast, abnormal grain growth occurs in the discontinuously co-sputtered film and grains grow to tens of micrometres (Fig. 2c), following the behaviour of pure Cu thin films [7,33,34]. This likely occurs due to the high Cu purity of the film-substrate interface in the initial stages of grain growth, which enhances the driving force for grain growth.

The black and red poles within the [111] pole-figures in Fig. 2 correspond to {111} diffraction peaks of Cu and {11 $\bar{2}$ 3} diffraction peaks of  $\alpha\text{-Al}_2\text{O}_3$ , respectively. The Cu pole figures imply that all the films exhibit a preferred (111) texture, similar to the pure Cu behaviour when deposited on c-sapphire [33,34]. Coupling the diffraction poles of

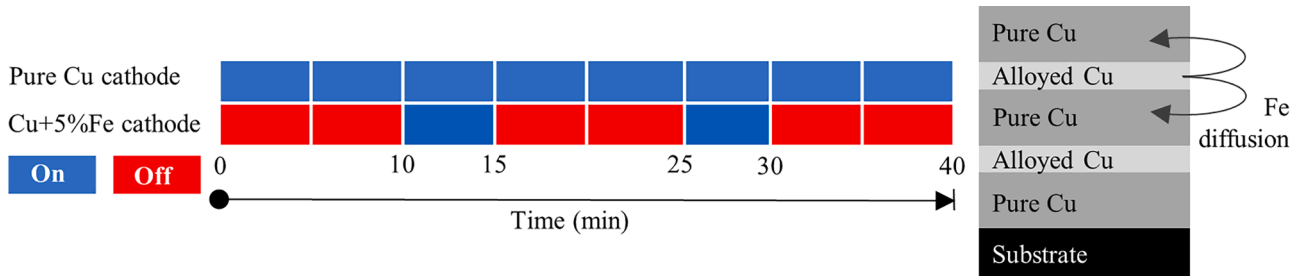


**Fig. 1.** The discontinuous sputtering protocol. A pure Cu target is active during the whole 40 min of deposition, while the alloyed target is operated twice for 5 mins. The resulting ‘multi-layered’ film is schematically presented to the right of the figure.

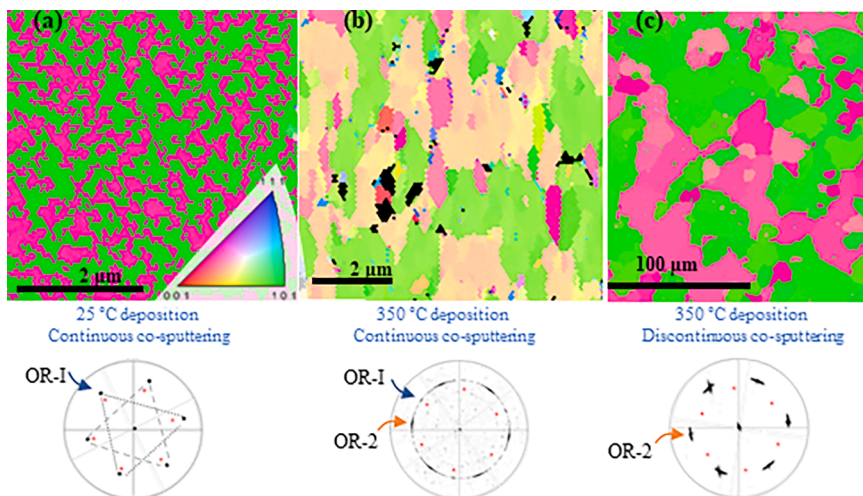


**Fig. 2.** In-plane EBSD resolved inverse pole figure maps and pole figures of the annealed films prepared by continuous sputtering at (a) 25°C and (b) 350°C, and (c) discontinuous sputtering at 350°C. Colours shown in the inverse pole figure maps indicate relative in-plane orientations as samples in (a,b) were differently oriented on the stage than the sample in (c). Black and red reflections in the [111] pole figures correspond to Cu and  $\alpha\text{-Al}_2\text{O}_3$ , respectively, and reveal the corresponding orientation relationship (OR).

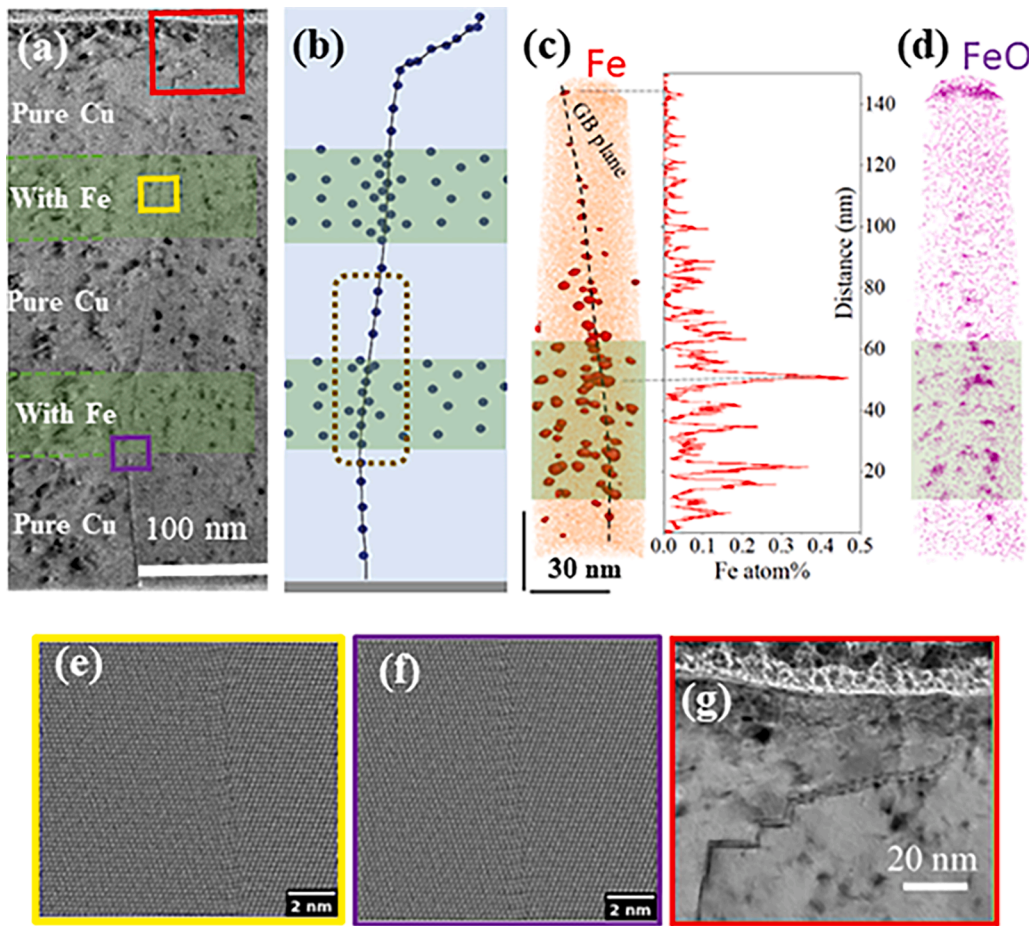


**Fig. 3.** (a) TEM resolved cross section of the discontinuously co-sputtered film after annealing (350°C, 3 hr) shows a columnar growth with a GB aligned along the film thickness. The dark contrast points originate from FIB induced defects [37]. The Fe-rich regions are marked with green colour. (b) Schematic illustration of the GB morphology and Fe content in the film. (c,d) APT reconstruction from the marked region in (b), Cu, Fe, and FeO atoms are shown in orange, red, and purple, respectively, with 0.1 at.% Fe iso-composition surfaces overlaid. The Fe content along the evaporation direction of the APT needle is presented. In atomically resolved HAADF-STEM images, no precipitates are observed in the (e) Fe-rich regions or at (f) interface between pure and alloyed layers. The exact locations are set based on the position along the film thickness. (g) Close to the film surface, the incoherent GB dissociates to coherent and incoherent segments.

Cu and Sapphire reveal the orientation relationships (ORs) between the film and the substrate [35]. The room temperature deposited film (film #1) has two Cu orientation variants rotated by 60° to form incoherent {211}  $\Sigma$ 3 GBs. The alignment of the {111} poles of Cu with {11 $\bar{2}$ 3} poles of  $\alpha$ -Al<sub>2</sub>O<sub>3</sub> indicates the OR {111}⟨01 $\bar{1}$ ⟩Cu || (0001)⟨10 $\bar{1}$ 0⟩ $\alpha$ -Al<sub>2</sub>O<sub>3</sub>, i.e. OR-I [35]. However, the {111} reflections of the 350°C continuously deposited film (film #2) are distributed on a ring having 70.5° inclination from the (111) pole in the middle of the circle. This indicates varying in-plane film orientations, still, one can recognise four main orientation variants; two Cu orientation variants rotated by 60° are aligned with the {11 $\bar{2}$ 3} reflections of  $\alpha$ -Al<sub>2</sub>O<sub>3</sub>, in a similar way as the former film (OR-I). Another two orientation variants are observed rotated by 60° from each other and by 30° from the {11 $\bar{2}$ 3}  $\alpha$ -Al<sub>2</sub>O<sub>3</sub> reflections, however these poles are smeared. These second two variants correspond to the OR {111}⟨01 $\bar{1}$ ⟩Cu || (0001)⟨2 $\bar{1}$  $\bar{1}$ 0⟩ $\alpha$ -Al<sub>2</sub>O<sub>3</sub>, known as OR-II [35], which has a larger angular in-plane spread as ORI. The OR-I and OR-II reflections are indicated by blue and orange arrows in Fig. 2.

A cross-section of the GB and grain interior of film #3 were inspected with high resolution transmission electron microscope (TEM) imaging. The sample was lifted out using a dual-beam SEM (Thermo Fisher Scientific Scios2HiVac). Thinning was performed using the Ga-ion beam, with final thinning parameters of 5 kV and 7.7 pA. Overview images the sample were investigated with a JEOL 2200 scanning TEM (S/TEM) instrument operating at 200 kV under bright field conditions. In order to resolve atomic scale images, a probe-corrected FEI Titan Themis 80-300 (Thermo Fisher Scientific) S/TEM. The atomically resolved high-angle annular dark-field (HAADF)-S/TEM images were registered with a HAADF detector (Fisheye Instruments Model 3000). Imaging, contrast optimisation, and filtering followed protocols described in Ref. [36].

The bright field TEM cross-sectional image of a  $\Sigma$ 3 GB (film #3) in

Fig. 3a shows a columnar grain structure with a boundary that deviates up to 7° from the surface normal, at depth of > 50 nm from the surface. The dark contrast region spots in Fig. 3a are focussed ion beam (FIB) artifacts. Atomically-resolved HAADF-STEM images show no precipitates within the film, at the boundary (Fig. 3e) or at the smooth interface between layers (Fig. 3f). The bright field TEM image in Fig. 3g (corresponding to the red rectangle location in Fig. 3a) shows that in the vicinity of the film surface the incoherent GB facets into coherent and incoherent segments. Such an observation might be caused by the fact that some GB structure variants are prone to adsorption more than others, leading to GB dissociation of the GB plane to lower the system energy as recently resolved for a  $\Sigma$ 5 GB in Cu-Ag [38,39]. Additionally, pinning of the GB at the surface might play a role in the near-surface behaviour of the GB.

For local chemical analysis, an APT tip was taken from the same film #3, in a way that it contains a GB in both alloyed and pure layers as marked by the dashed rectangle in Fig. 3b. FIB lift-out and annular milling techniques were employed to prepare needle-shaped geometry APT specimens in a FEI Helios Nanolab 600i [40]. The specimens were analysed in a Cameca Instruments Local Electrode Atom Probe (LEAP) 5000 XS operated at a specimen set point temperature of 40 K and laser pulse energy of 30 pJ at a pulse repetition rate of 200 kHz and an average of 5 ions detected per 1000 pulse detection rate. The APT data was reconstructed using the AP Suite 6.1, while compositions were measured using the peak decomposition algorithm from the software.

The APT results in Fig. 3(c,d) show that the Fe accumulates in spheroidal clusters with a matrix composition of 40±5 ppm Fe, which are partially mono-oxidized. These clusters might be an early stage of a nucleation of Fe in Cu, similarly to the findings of Cu precipitation in Fe matrix [41–44]. Fe exhibits a strong clustering behaviour rather than a

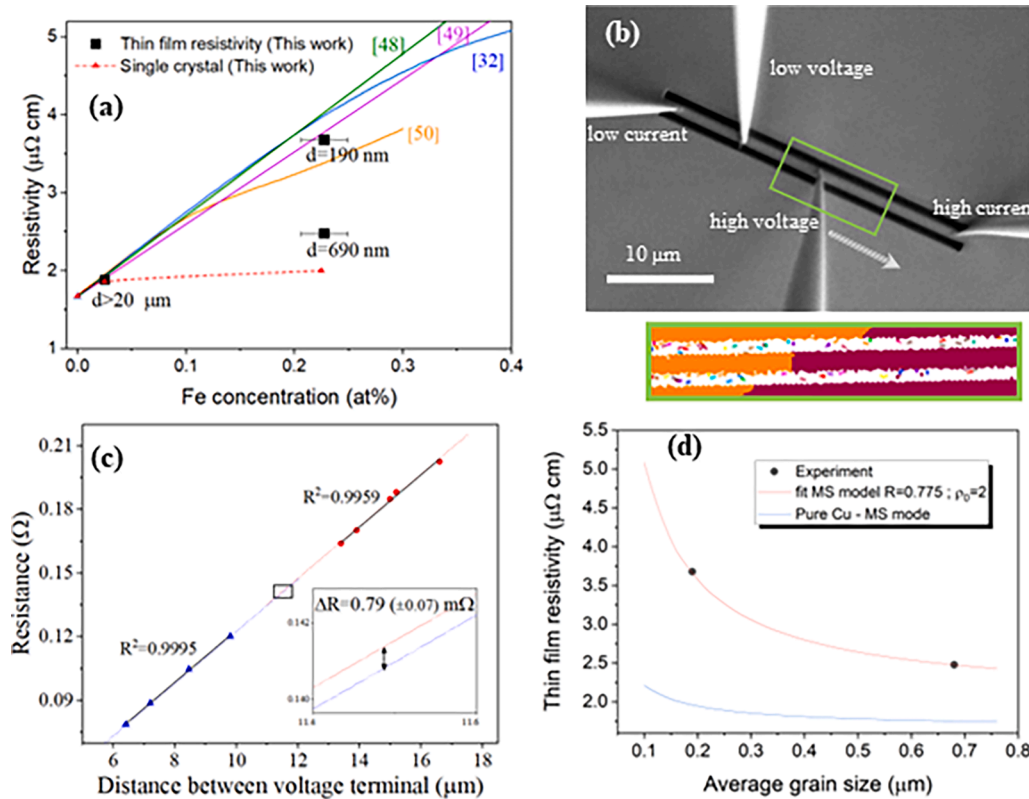


**Fig. 4.** (a) The macroscopic-level measured resistivity of the films is given in black squares. The single crystal resistivities are given by triangles and red dashed line. Solid lines represent resistivity values and trends from literature [32,48–50]. (b) GB resistivity measurement on a bi-crystal conduction line using four independent micromanipulators, the high voltage needle moves along the direction indicated by an arrow to cross the GB EBSD-resolved grain map of the GB region. (c) The jump in resistance measured in the scanning resistance measurements is utilised in calculation of  $\gamma_{GB}$ . (d) Fitting MS model to the 0.25 at.% Fe-alloyed Cu in presented in red. The blue curve shows the MS curve of pure Cu for reference.

**Table 2**

Comparison between measured single crystal resistivity of Cu (Fe-free) and Fe-alloyed Cu with nominal composition of 0.025 at.% Fe. Error bars in resistivity are  $\pm 0.02 \mu\Omega \text{ cm}$ .

	Pure Cu	Fe-alloyed Cu	Resistivity increase
Single crystal resistivity ( $\mu\Omega \text{ cm}$ )	1.67 ( $\pm 0.02$ )	1.86 ( $\pm 0.02$ )	11 %
{211} $\Sigma$ 3 GB resistivity ( $\mu\Omega \text{ cm}^2$ )	1.1 ( $\pm 0.1$ )	11.5 ( $\pm 1$ )	$\sim 1000$ %

statistical randomisation as deduced from analysing the APT data with the maximum separation method [45–47] – the analysis is explained in the Supplementary Materials. No excess of contaminations is found either inside the grain or at the GBs (see Figs. S2,S3 and Table S1 –within the Supplementary Material). A minor quantity of Ga ions is observed as FIB damage, and Ga is not enriched at the boundary. APT measurements confirm the distinct Fe concentration between the Fe-rich layers and pure Cu layers. The overall composition in the grain interior of the Fe-rich layer is 0.1 at.% (1000 ppm), and  $\sim 40$  ppm in the pure Cu layer. Since the volume fraction of the alloyed layers is one quarter of the total film, then the overall composition can be estimated at 0.025 at.% Fe (250 ppm). The APT data in Fig. 3c provides a strong indication of Fe diffusion along the GB, which fits the diffusion length calculated for the specific annealing conditions –6  $\mu\text{m}$  in GBs, as presented in the Supplementary Material.

The global film resistivities were inspected by Van-der-Pauw method, following the methodology described in Ref. [18]. Resistivity of the films are presented in Fig. 4 as black squares. The resistivity of the film having a composition of 0.25 at.% Fe and an average grain size of 190 nm is  $3.68 \pm 0.01 \mu\Omega \text{ cm}$ , coinciding with values reported in literature [32,48–50], as shown in Fig. 4a. However, increasing the average grain size of the film to 690 nm at the same global composition by the higher deposition temperature of 350°C decreases the room temperature resistivity to  $2.75 \pm 0.01 \mu\Omega \text{ cm}$  – a lower value than reported in literature (Fig. 4). This behaviour is attributed to annealing out deposition

defects. The resistivity of the film having a composition of 0.025 at.% Fe and an average grain size of tens of microns is  $1.88 \pm 0.01 \mu\Omega \text{ cm}$ . However, resistivity within single grains (single crystal) of the 0.025 at.% Fe film is only  $1.86 \pm 0.01 \mu\Omega \text{ cm}$ , indicating the small contribution of GBs to resistivity when the average grain size is tens of microns.

In addition to the global resistivity, the single crystal and individual GB resistivities of the discontinuously-sputtered (film #3, due to its large grain-size) film were directly measured inside a SEM (Gemini, Zeiss) using four micromanipulators-driven needles (PS4, Kleindiek). Experimental details follow the work done in Ref. [18]. The grain interior resistivity was measured through linear four-point probe inside a  $\sim 100 \mu\text{m}$  grain, while the spacing between neighbouring needles was set to 10  $\mu\text{m}$ . Fig. 5a shows a SEM frame during the local electrical measurement over a GB segment, which is characterised by EBSD (Fig. 5b). The GB resistivity is obtained from the jump in measured resistance when the voltage measurement crosses the GB [18], as illustrated in Fig. 5c.

The measured resistivity for a single crystal Cu alloyed with 0.025 at.% Fe (film #3) is  $1.86 \pm 0.02 \mu\Omega \text{ cm}$ , corresponding to an increase of  $\sim 11\%$  from pure Cu as indicated in Table 2, which is discussed in discussed in Ref. [7]. However, the resistivity of an individual  $\Sigma 3\{211\}$  GB is  $11.5 \mu\Omega \text{ cm}^2$ , which is a factor of 10 higher than the value measured for pure Cu GB discussed in Ref. [7], due to the GB enrichment with Fe. The measured increase of  $\gamma_{GB}$  in the enriched GBs exceed the DFT predictions [12], since the reported calculations relate to solute atoms at

**Table 3**

Single crystal resistivity and GB reflection coefficient of pure and 0.25 at.% Fe-alloyed Cu.  $R$  for pure Cu is taken from Ref. [15].

	Pure Cu	Fe-alloyed
Single crystal resistivity ( $\mu\Omega\text{ cm}$ )	1.67	2.00
GB reflection coefficient	0.46	0.775

the boundary plane, whereas the GB enrichment in the Cu-Fe system the occurs as Fe and FeO clusters. The clustering has several impacts on the calculation; the chemical bonds are defined differently from the segregation case, and hence the electronic structure is affected. In addition, the clusters act as additional scattering centres. The GB resistivity calculation considers a 10% increase in the GB cross-section compared to the conduction line's cross-section – as deduced from the TEM image in Fig. 3a. The effect of the of the near-surface faceted GB segment on the calculated GB resistivity is thought to be negligible due to their low fraction, and because they are aligned in the direction of electrons flow which minimises their scattering cross-section, and because the coherent  $\Sigma 3$  has even lower GB resistivity than the incoherent  $\Sigma 3$  [51–53]. Only the  $\Sigma 3$  GB was inspected here, since it is the only type which is not grooved. The other GB types exhibit grooving, likely due to their higher interfacial energies [7], which affects the measured resistance due to surface scattering.

To acquire the value of GB reflection coefficient  $R$  no abnormal grain growth is required, but two samples with similar composition and distinct grain size – films #1 and #2 satisfy this condition with a composition of 0.25 ( $\pm 0.05$ ) at.% Fe – deduced from APT analysis (shown in the Supplementary Material). A Mayadas-Shatzkes (MS) model is then applied to analyse the GB contribution to resistivity [17]. Within this model, the electron mean free path of the alloy  $l_0$  is unknown. However, one can assume, based on the Drude model, that the electron mean free path for the alloy is inverse to its resistivity  $\rho_0$ , or simply  $l_0 = l_{Cu} \cdot (\rho_{Cu} / \rho_0)$  with mean free path of  $l_{Cu} = 39.9\text{ nm}$  and resistivity  $\rho_{Cu} = 1.67\text{ }\mu\Omega\text{cm}$  for pure Cu [54]. Fig. 6 shows the data fitting the MS model to the experimental data. The fitted single crystal and GB resistivities are listed in Table 3. The GB resistivity is manifested by a high  $R$  - a steep slope of the alloys' curve compared to the pure Cu curve in Fig. 6. Relevant parameters of the pure Cu are taken from Ref. [15]. This implies that GBs dominate the resistivity in nanocrystalline alloys, while the increase in a single crystal alloy is less significant than previously reported in literature as evident from Fig. 4.

In summary, the electrical properties of thin film Fe-alloyed Cu systems were studied in the context of decoupling the resistivity contributions of both grain interior and grain boundaries. Fe-diluted Cu thin films were prepared by a co-sputtering technique, where abnormal grain growth of the thin films was achieved by controlling the deposition process. Fe is distributed in confined Fe-rich clusters, with no observed atomic segregation. Alloying Cu with nominally 0.025 at.% Fe leads to a significant increase by a factor of 10 in the GB resistivity, while the grain interior resistivity is only raised by a factor of 0.1. This work implies that GBs are the main contributors to the high resistivity of these alloys, while manipulating the resistivity can be done by thin film deposition processes.

### Declaration of Competing Interest

The authors declare that they have no known competing financial interests or personal relationships that could have appeared to influence the work reported in this paper.

### Acknowledgments

H.B, L.L, and G.D. acknowledge the financial support by the ERC Advanced Grant GB CORRELATE (Grant Agreement 787446 GB-CORRELATE).

### Supplementary materials

Supplementary material associated with this article can be found, in the online version, at doi:10.1016/j.scriptamat.2023.115393.

### References

- [1] H. Ye, X. Cui, X. Li, H. Cui, B. Zhang, H. Li, Y. Pan, R. Feng, Y. Wu, X. Liu, Fabrication of hypoeutectic Al-4Si alloy with high electrical conductivity, high plasticity and medium strength by the dual treatment of Al matrix and eutectic Si microstructure, *J. Alloys Compd.* 885 (2021), 161117, <https://doi.org/10.1016/j.jallcom.2021.161117>.
- [2] X. Cui, Y. Wu, G. Zhang, Y. Liu, X. Liu, Study on the improvement of electrical conductivity and mechanical properties of low alloying electrical aluminum alloys, *Compos. B Eng.* 110 (2017) 381–387, <https://doi.org/10.1016/j.compositesb.2016.11.042>.
- [3] X. Guo, Z. Xiao, W. Qiu, Z. Li, Z. Zhao, X. Wang, Y. Jiang, Microstructure and properties of Cu-Cr-Nb alloy with high strength, high electrical conductivity and good softening resistance performance at elevated temperature, *Mater. Sci. Eng.* 749 (2019) 281–290, <https://doi.org/10.1016/j.msea.2019.02.036>.
- [4] M.Y. Murashkin, I. Sabirov, X. Sauvage, R.Z. Valiev, Nanostructured Al and Cu alloys with superior strength and electrical conductivity, *J. Mater. Sci.* 51 (2016) 33–49, <https://doi.org/10.1007/s10853-015-9354-9>.
- [5] S.N. Khaghholi, M. Javidani, A. Maltais, X.G. Chen, Review on recent progress in Al–Mg–Si 6xxx conductor alloys, *J. Mater. Res.* 37 (2022) 670–691, <https://doi.org/10.1557/s43578-022-00488-3>.
- [6] J.P. Hou, R. Li, Q. Wang, H.Y. Yu, Z.J. Zhang, Q.Y. Chen, H. Ma, X.M. Wu, X.W. Li, Z.F. Zhang, Breaking the trade-off relation of strength and electrical conductivity in pure Al wire by controlling texture and grain boundary, *J. Alloys Compd.* 769 (2018) 96–109, <https://doi.org/10.1016/j.jallcom.2018.07.358>.
- [7] H. Bishara, S. Lee, T. Brink, M. Ghidelli, G. Dehm, Understanding grain boundary electrical resistivity in Cu: the effect of boundary structure, *ACS Nano* 15 (2021) 16607–16615, <https://doi.org/10.1021/acsnano.1c06367>.
- [8] K. Barmak, A. Darbal, K.J. Ganesh, P.J. Ferreira, J.M. Rickman, T. Sun, B. Yao, A. P. Warren, K.R. Coffey, Surface and grain boundary scattering in nanometric Cu thin films: a quantitative analysis including twin boundaries, *J. Vac. Sci. Technol. A* 32 (2014) 61503, <https://doi.org/10.1116/1.4894453>.
- [9] I. Bakonyi, V.A. Isnaini, T. Kolonits, Zs. Czizgany, J. Gubicza, L.K. Varga, E. Tóth-Kádár, L. Pogány, L. Péter, H. Ebert, The specific grain-boundary electrical resistivity of Ni, *Philos. Mag.* 99 (2019) 1139–1162, <https://doi.org/10.1080/14786435.2019.1580399>.
- [10] M. César, D. Liu, D. Gall, H. Guo, Calculated resistances of single grain boundaries in copper, *Phys. Rev. Appl.* 2 (2014) 44007, <https://doi.org/10.1103/PhysRevApplied.2.044007>.
- [11] D. Gall, The search for the most conductive metal for narrow interconnect lines, *J. Appl. Phys.* 127 (2020) 50901, <https://doi.org/10.1063/1.5133671>.
- [12] M. César, D. Gall, H. Guo, Reducing grain-boundary resistivity of copper nanowires by doping, *Phys. Rev. Appl.* 5 (2016) 54018, <https://doi.org/10.1103/PhysRevApplied.5.054018>.
- [13] Y. Wang, L. Zhu, G. Niu, J. Mao, Conductive Al alloys: the contradiction between strength and electrical conductivity, *Adv. Eng. Mater.* 23 (2021), 2001249, <https://doi.org/10.1002/adem.202001249>.
- [14] X. Sauvage, E. v Bobruk, M.Yu. Murashkin, Y. Nasedkina, N.A. Enikeev, R. Z. Valiev, Optimization of electrical conductivity and strength combination by structure design at the nanoscale in Al–Mg–Si alloys, *Acta Mater.* 98 (2015) 355–366, <https://doi.org/10.1016/j.actamat.2015.07.039>.
- [15] I. Bakonyi, Accounting for the resistivity contribution of grain boundaries in metals: critical analysis of reported experimental and theoretical data for Ni and Cu, *The European Physical Journal Plus* 136 (2021) 410, <https://doi.org/10.1140/epjp/s13360-021-01303-4>.
- [16] P. v Andrews, Resistivity due to grain boundaries in pure copper, *Phys. Lett.* 19 (1965) 558–560, [https://doi.org/10.1016/0031-9163\(65\)90776-6](https://doi.org/10.1016/0031-9163(65)90776-6).
- [17] A.F. Mayadas, M. Shatzkes, Electrical-RESISTIVITY MODEL FOR POLYCRYSTALLINE FILMS: THE CASE OF ARBITRARY REFLECTION AT EXTERNAL SURFACES, *Phys. Rev. B* 1 (1970) 1382–1389, <https://doi.org/10.1103/PhysRevB.1.1382>.
- [18] H. Bishara, M. Ghidelli, G. Dehm, Approaches to measure the resistivity of grain boundaries in metals with high sensitivity and spatial resolution: a case study employing Cu, *ACS Appl. Electron. Mater.* 2 (2020) 2049–2056, <https://doi.org/10.1021/acsaem.0c00311>.
- [19] J. Greiser, P. Müllner, E. Arzt, Abnormal growth of “giant” grains in silver thin films, *Acta Mater.* 49 (2001) 1041–1050, [https://doi.org/10.1016/S1359-6454\(00\)00372-4](https://doi.org/10.1016/S1359-6454(00)00372-4).
- [20] P. Sonnweber-Ribic, P.A. Gruber, G. Dehm, H.P. Strunk, E. Arzt, Kinetics and driving forces of abnormal grain growth in thin Cu films, *Acta Mater.* 60 (2012) 2397–2406, <https://doi.org/10.1016/j.actamat.2011.12.030>.
- [21] K. Barmak, E. Eggeling, R. Sharp, S. Roberts, T. Shyu, T. Sun, B. Yao, S. Ta'asan, D. Kinderlehrer, A.D. Rollett, K. Coffey, Grain growth and the puzzle of its stagnation in thin films: a detailed comparison of experiments and simulations, *Mater. Sci. Forum* 715–716 (2012) 473–479, <https://doi.org/10.4028/www.scientific.net/MSF.715-716.473>.
- [22] C.V. Thompson, Grain growth in thin films, *Annu. Rev. Mater. Sci.* 20 (1990) 245–268.

- [23] Y. Addab, M.K. Kini, B. Courtois, A. Savan, A. Ludwig, N. Bozzolo, C. Scheu, G. Dehm, D. Chatain, Microstructure evolution and thermal stability of equiatomic CoCrFeNi films on (0001)  $\alpha$ -Al<sub>2</sub>O<sub>3</sub>, *Acta Mater.* 200 (2020) 908–921, <https://doi.org/10.1016/j.actamat.2020.09.064>.
- [24] A. Sharma, A. Kumar, N. Gazit, D.J. Srolovitz, E. Rabkin, Grain growth and solid-state dewetting of Bi-Crystal Ni-Fe thin films on sapphire, *Acta Mater.* 168 (2019) 237–249, <https://doi.org/10.1016/j.actamat.2019.02.015>.
- [25] H.P. Longworth, C. v Thompson, Abnormal grain growth in aluminum alloy thin films, *J. Appl. Phys.* 69 (1991) 3929–3940, <https://doi.org/10.1063/1.348452>.
- [26] J.M.E. Harper, J. Gupta, D.A. Smith, J.W. Chang, K.L. Holloway, C. Cabral, D. P. Tracy, D.B. Knorr, Crystallographic texture change during abnormal grain growth in Cu-Co thin films, *Appl. Phys. Lett.* 65 (1994) 177–179, <https://doi.org/10.1063/1.112664>.
- [27] H. Yu, Y. Zeng, R. Hong, Influence of Fe addition on the microstructure and mechanical properties of Cu alloys, *Mater. Sci.* 3 (2021), <https://doi.org/10.35702/msci.10010>.
- [28] J.M. Denney, Precipitate kinetics and structure in a Cu-2.4% Fe alloy, *Acta Metall.* 4 (1956) 586–592, [https://doi.org/10.1016/0001-6160\(56\)90161-4](https://doi.org/10.1016/0001-6160(56)90161-4).
- [29] Y. Tsunoda, N. Kunitomi, Structural phase transition of  $\gamma$ -Fe precipitates in Cu, *J. Phys. F Met. Phys.* 18 (1988) 1405–1420, <https://doi.org/10.1088/0305-4608/18/7/010>.
- [30] S.C. Abrahams, L. Guttman, J.S. Kasper, Neutron diffraction determination of antiferromagnetism in face-centered cubic ( $\gamma$ ) iron, *Phys. Rev.* 127 (1962) 2052–2055, <https://doi.org/10.1103/PhysRev.127.2052>.
- [31] U. Gonser, C.J. Meechan, A.H. Muir, H. Wiedersich, Determination of Néel Temperatures in fcc Iron, *J. Appl. Phys.* 34 (1963) 2373–2378, <https://doi.org/10.1063/1.1702749>.
- [32] G. Kim, X. Chai, L. Yu, X. Cheng, D.S. Gianola, Interplay between grain boundary segregation and electrical resistivity in dilute nanocrystalline Cu alloys, *Scr. Mater.* 123 (2016) 113–117, <https://doi.org/10.1016/j.scriptamat.2016.06.008>.
- [33] G. Dehm, M. Rühle, G. Ding, R. Raj, Growth and structure of copper thin films deposited on (0001) sapphire by molecular beam epitaxy, *Philos. Mag. B* 71 (1995) 1111–1124, <https://doi.org/10.1080/01418639508241899>.
- [34] S.H. Oh, C. Scheu, T. Wagner, M. Rühle, Control of bonding and epitaxy at copper/sapphire interface, *Appl. Phys. Lett.* 91 (2007), 141912, <https://doi.org/10.1063/1.2794025>.
- [35] G. Dehm, H. Edongué, T. Wagner, S. Oh, E. Arzt, Obtaining different orientation relationships for Cu Films grown on (0001)  $\alpha$ -Al<sub>2</sub>O<sub>3</sub> substrates by magnetron sputtering, *Zeitschrift Fur Metallkunde* 96 (2005) 249–254.
- [36] L. Frommeyer, T. Brink, R. Freitas, T. Frolov, G. Dehm, C.H. Liebscher, Dual phase patterning during a congruent grain boundary phase transition in elemental copper, *Nat. Commun.* 13 (2022) 3331, <https://doi.org/10.1038/s41467-022-30922-3>.
- [37] D. Kiener, Z. Zhang, S. Šturm, S. Cazottes, P.J. Imrich, C. Kirchlechner, G. Dehm, Advanced nanomechanics in the TEM: effects of thermal annealing on FIB prepared Cu samples, *Philos. Mag.* 92 (2012) 3269–3289, <https://doi.org/10.1080/14786435.2012.685966>.
- [38] N.J. Peter, T. Frolov, M.J. Duarte, R. Hadian, C. Ophus, C. Kirchlechner, C. H. Liebscher, G. Dehm, Segregation-induced nanofaceting transition at an asymmetric tilt grain boundary in copper, *Phys. Rev. Lett.* 121 (2018), 255502, <https://doi.org/10.1103/PhysRevLett.121.255502>.
- [39] N.J. Peter, M.J. Duarte, C. Kirchlechner, C.H. Liebscher, G. Dehm, Faceting diagram for Ag segregation induced nanofaceting at an asymmetric Cu tilt grain boundary, *Acta Mater.* 214 (2021), 116960, <https://doi.org/10.1016/j.actamat.2021.116960>.
- [40] K. Thompson, D. Lawrence, D.J. Larson, J.D. Olson, T.F. Kelly, B. Gorman, In situ site-specific specimen preparation for atom probe tomography, *Ultramicroscopy* 107 (2007) 131–139, <https://doi.org/10.1016/j.ultramicro.2006.06.008>.
- [41] A. Heinrich, T. Al-Kassab, R. Kirchheim, Investigation of the early stages of decomposition of Cu–0.7at.% Fe with the tomographic atom probe, *Mater. Sci. Eng.* 353 (2003) 92–98, [https://doi.org/10.1016/S0921-5093\(02\)00673-1](https://doi.org/10.1016/S0921-5093(02)00673-1).
- [42] M.K. Miller, B.D. Wirth, G.R. Odette, Precipitation in neutron-irradiated Fe–Cu and Fe–Cu–Mn model alloys: a comparison of APT and SANS data, *Mater. Sci. Eng.* 353 (2003) 133–139, [https://doi.org/10.1016/S0921-5093\(02\)00679-2](https://doi.org/10.1016/S0921-5093(02)00679-2).
- [43] S. Ahlawat, S.K. Sarkar, D. Sen, A. Biswas, Revisiting temporal evolution of Cu-rich precipitates in Fe–Cu alloy: correlative small angle neutron scattering and atom-probe tomography studies, *Microsc. Microanal.* 25 (2019) 840–848, <https://doi.org/10.1017/S1431927619000515>.
- [44] D. Isheim, M.S. Gagliano, M.E. Fine, D.N. Seidman, Interfacial segregation at Cu-rich precipitates in a high-strength low-carbon steel studied on a sub-nanometer scale, *Acta Mater.* 54 (2006) 841–849, <https://doi.org/10.1016/j.actamat.2005.10.023>.
- [45] L.T. Stephenson, M.P. Moody, P. v Liddicoat, S.P. Ringer, New techniques for the analysis of fine-scaled clustering phenomena within atom probe tomography (APT) data, *Microsc. Microanal.* 13 (2007) 448–463, <https://doi.org/10.1017/S1431927607070900>.
- [46] E.A. Marquis, J.M. Hyde, Applications of atom-probe tomography to the characterisation of solute behaviours, *Mater. Sci. Eng.* 69 (2010) 37–62, <https://doi.org/10.1016/j.mser.2010.05.001>.
- [47] Y. Chen, P.H. Chou, E.A. Marquis, Quantitative atom probe tomography characterization of microstructures in a proton irradiated 304 stainless steel, *J. Nucl. Mater.* 451 (2014) 130–136, <https://doi.org/10.1016/j.jnucmat.2014.03.034>.
- [48] W.B. Pearson, CIII. Electron transport in copper and dilute alloys at low temperature, London, Edinburgh, Dublin Philosoph. Magazine J. Sci. 46 (1955) 911–919, <https://doi.org/10.1080/14786440808561244>.
- [49] J.O. Linde, Elektrische Eigenschaften verdünnter Mischkristalllegierungen III. Widerstand von Kupfer- und Goldlegierungen. Gesetzmäßigkeiten der Widerstandserhöhungen, *Ann. Phys.* 407 (1932) 219–248, <https://doi.org/10.1002/andp.19324070206>.
- [50] C.A. Domenicali, E.L. Christenson, Effects of transition metal solutes on the electrical resistivity of copper and gold between 4° and 1200°K, *J. Appl. Phys.* 32 (1961) 2450–2456, <https://doi.org/10.1063/1.1777090>.
- [51] L. Lu, Y. Shen, X. Chen, L. Qian, K. Lu, Ultrahigh strength and high electrical conductivity in copper, *Science* 304 (2004) 422, <https://doi.org/10.1126/science.1092905> (1979)LP –426.
- [52] T. Sun, B. Yao, A.P. Warren, K. Barmak, M.F. Toney, R.E. Peale, K.R. Coffey, Dominant role of grain boundary scattering in the resistivity of nanometric Cu films, *Phys. Rev. B* 79 (2009) 41402, <https://doi.org/10.1103/PhysRevB.79.041402>.
- [53] K. Barmak, S. Ezzat, R. Gusley, A. Jog, S. Kerdsonpanya, A. Khaniya, E. Milosevic, W. Richardson, K. Sentosun, A. Zangiabadi, D. Gall, W.E. Kaden, E.R. Mucciolo, P. K. Schelling, A.C. West, K.R. Coffey, Epitaxial metals for interconnects beyond Cu, *J. Vac. Sci. Technol. A* 38 (2020) 33406, <https://doi.org/10.1116/6.0000018>.
- [54] D. Gall, Electron mean free path in elemental metals, *J. Appl. Phys.* 119 (2016) 85101, <https://doi.org/10.1063/1.4942216>.